



HAL
open science

Measurement of magnetic field fluctuations in the Parker Solar Probe and Solar Orbiter missions

G. Jannet, Thierry Dudok de Wit, Vladimir Krasnoselskikh, Matthieu Kretzschmar, P. Ferreau, M. Bergerard-timofeeva, Clemence Agrapart, Jean-Yves Brochot, Gilles Chalumeau, P. Martin, et al.

► **To cite this version:**

G. Jannet, Thierry Dudok de Wit, Vladimir Krasnoselskikh, Matthieu Kretzschmar, P. Ferreau, et al. Measurement of magnetic field fluctuations in the Parker Solar Probe and Solar Orbiter missions. *Journal of Geophysical Research Space Physics*, 2021, 126 (2), pp.e2020JA028543. 10.1029/2020JA028543 . insu-03085892v2

HAL Id: insu-03085892

<https://insu.hal.science/insu-03085892v2>

Submitted on 29 Mar 2021

HAL is a multi-disciplinary open access archive for the deposit and dissemination of scientific research documents, whether they are published or not. The documents may come from teaching and research institutions in France or abroad, or from public or private research centers.

L'archive ouverte pluridisciplinaire **HAL**, est destinée au dépôt et à la diffusion de documents scientifiques de niveau recherche, publiés ou non, émanant des établissements d'enseignement et de recherche français ou étrangers, des laboratoires publics ou privés.

JGR Space Physics

RESEARCH ARTICLE

10.1029/2020JA028543

Key Points:

- The search-coil magnetometer (SCM) measures AC magnetic fields onboard the Parker Solar Probe and Solar Orbiter satellites
- This instrument is important for addressing the problem of coronal heating, solar wind formation and particle acceleration by means of wave mode identification
- Both SCM instruments have been launched and are now operating

Correspondence to:

G. Jannet,
guillaume.jannet@cnrs-orleans.fr

Citation:

Jannet, G., Dudok de Wit, T., Krasnoselskikh, V., Kretzschmar, M., Ferreau, P., Bergerard-Timofeeva, M., et al. (2021). Measurement of magnetic field fluctuations in the Parker Solar Probe and Solar Orbiter missions. *Journal of Geophysical Research: Space Physics*, 126, e2020JA028543. <https://doi.org/10.1029/2020JA028543>

Received 24 AUG 2020
 Accepted 25 NOV 2020

© 2020. American Geophysical Union.
 All Rights Reserved.

Measurement of Magnetic Field Fluctuations in the Parker Solar Probe and Solar Orbiter Missions

G. Jannet¹, T. Dudok de Wit¹ , V. Krasnoselskikh¹, M. Kretzschmar¹, P. Ferreau¹, M. Bergerard-Timofeeva^{1,2}, C. Agrapart¹, J.-Y. Brochot¹, G. Chalumeau¹, P. Martin¹, C. Revillet¹, S. D. Bale^{3,4,5,6} , M. Maksimovic⁷, T. A. Bowen³, C. Brysbaert⁸, K. Goetz⁹, E. Guilhem¹⁰, P. R. Harvey³, V. Leray^{1,11}, and E. Lorfèvre⁸

¹LPC2E, CNRS, CNES and University of Orléans, Orléans, France, ²HUTCHINSON SA Centre de Recherche et d'Innovation, Paris, France, ³Space Sciences Laboratory, University of California, Berkeley, CA, USA, ⁴Physics Department, University of California, Berkeley, CA, USA, ⁵The Blackett Laboratory, Imperial College London, London, UK, ⁶School of Physics and Astronomy, Queen Mary University of London, London, UK, ⁷LESIA, Observatoire de Paris, Université PSL, CNRS, Sorbonne Université, Université de Paris, Paris, France, ⁸CNES, Toulouse, France, ⁹School of Physics and Astronomy, University of Minnesota, Minneapolis, MN, USA, ¹⁰Altran Sud Ouest, Blagnac, France, ¹¹HENSOLDT Space Consulting, GOLF PARK - Bâtiment F, 1 Rond-point Du Général Eisenhower, Toulouse, France

Abstract The search-coil magnetometer (SCM) measures the magnetic signature of solar wind fluctuations with three components in the 3 Hz–50 kHz range and one single component in the 1 kHz–1 MHz range. This instrument is important for providing in situ observations of transients caused by interplanetary shocks and reconnection, for the identification of electromagnetic wave modes in plasmas and the determination of their characteristics (planarity, polarization, ellipticity, and *k*-vector) and for studying the turbulent cascade in the kinetic range. Two similar triaxial search-coils have been built for the Parker Solar Probe and Solar Orbiter missions. Here we describe the science objectives of both missions which led to the SCM design and present the characteristics of the two instruments.

1. Introduction

Recently, two major space missions have been launched with the aim of better understanding the highly dynamic inner heliosphere and the influence on it of the Sun. This largely unexplored region of our solar system continuously affects our near-Earth environment and also challenges us with some of the major unsolved questions in contemporary physics (Viall & Borovsky, 2020).

These missions are: Parker Solar Probe (NASA), launched in August 2018 and Solar Orbiter (ESA/NASA) launched in February 2020. The main objective of Solar Orbiter is to determine how the Sun creates and controls the heliosphere (Müller et al., 2013). Answering this question requires to relate the in situ measurements back to their source regions and to remotely characterize these source regions. For this, Solar Orbiter will go as close as 0.28 AU from the Sun and up 28° in heliolatitude for the nominal mission and 34° for the extended mission. Solar Orbiter embarks six remote sensing and four *in situ* experiments.

Parker Solar Probe shares similar objectives, with a greater focus on the mechanisms that heat and accelerate the solar wind (Fox et al., 2015). While the perihelion of Solar Orbiter is at 0.28 AU or 60.2 solar radii from the Sun, which corresponds to the orbit of Mercury, Parker Solar Probe will get as close as 0.0459 AU or 9.86 solar radii and will therefore be the first mission to literally enter the solar corona. Parker Solar Probe embarks a heliospheric imager and three *in situ* experiments to characterize the electromagnetic fields and particles. These missions were preceded in the 1980s by the twin HELIOS spacecraft (Porsche, 1981), which, for a long time, were the objects that had come closest to the Sun, with a perihelion of 0.29 AU.

Both Parker Solar Probe and Solar Orbiter carry a search-coil magnetometer (SCM) to study the magnetic component of electromagnetic waves. These search-coils were built at the Laboratoire de Physique et Chimie de l'Environnement et de l'Espace (LPC2E, CNRS, CNES & University of Orleans). Both have a long heritage whose latest instrument flew DEMETER (Parrot et al., 2006). A similar one should launch in 2020 on TARANIS (Lefeuvre et al., 2008).

The SCM measures magnetic field fluctuations typically between 1 Hz and 1 MHz (see below for more details). On Parker Solar Probe, the SCM is part of the FIELDS instrumental suite (Bale et al., 2016), whose instruments measure magnetic fields from DC up to 1 MHz and electric fields from DC up to 19.2 MHz. On Solar Orbiter, the SCM is part of the Radio and Plasma Waves (RPW) suite (Maksimovic et al., 2020), which performs similar measurements.

In this paper, we concentrate on the scientific requirements and design of the SCM for the two inner heliospheric missions. At the time of writing, both spacecraft are operating and have already provided a wealth of interesting data.

2. Science Requirements

The primary role of the SCM is to provide, together with other instruments, a thorough description of the physical properties of fluctuations in the solar wind. There are a number of reasons for which the characterization of magnetic fields variations at these frequencies is of great interest. First, Alfvén turbulence and ion-cyclotron waves (ICW) are supposed to play an important role in the heating and acceleration of the solar wind. Recent studies of the particle distributions measured onboard HELIOS have evidenced the impact of pitch angle diffusion of protons (Tu & Marsch, 2001), which suggests that Alfvén turbulence and ICW activity continue to heat the plasma close to the Sun. These waves are generated below and at the local proton gyrofrequency, respectively. At 0.2 AU, the ion gyro-frequency is typically 1 Hz (Gurnett, 1978). The corresponding frequencies observed in the spacecraft frame can be Doppler shifted to the kHz range. Alfvén and ICW, whose minimum amplitude should be of the order of $10^{-2} \text{ nT} / \sqrt{\text{Hz}}$, can be measured by the SCM.

In the close vicinity of the Sun, the electron distribution function has three components: core, halo, and strahl (Pierrard et al., 2001). The energy of the halo and strahl populations ranges from several tens of eV up to several hundreds of eV. Their main features are an isotropic angular distribution for halo electrons, and a very narrow angular distribution along the magnetic field lines for the strahl population. The latter is not observed at large distances from the Sun; observations from Ulysses have shown that it vanishes beyond 5 AU. This has led to the idea that the halo distribution is fueled by the strahl population. Electromagnetic waves and in particular whistler waves are key candidates for such energy exchange.

Our ability to detect these different types of waves is summarized in Figure 1 in which we compare their amplitude in the inner heliosphere with the sensitivity of the instrument. This sensitivity is set by the noise level of the instrument and determines the minimum level below which the wave amplitude is too weak to be detected.

Ion-acoustic waves are also expected to play a significant role in the plasma heating and dynamics. The next resonant frequency above the proton gyro-frequency f_{cp} is the electron gyro-frequency ($f_{ce} = 2 \text{ kHz}$ at 0.2 AU). For frequencies between f_{cp} and f_{ce} the only electromagnetic mode that can propagate is the right-hand polarized whistler mode. However, other types of waves such kinetic Alfvén waves, when Doppler shifted, may be observed in the same frequency range. A measurement of both the magnetic and electric field vectors is necessary to distinguish between these different wave modes. Observations made by HELIOS have shown that whistler turbulence is present in the solar wind at frequencies up to f_{ce} (Jagarlamudi et al., 2020) with a tendency for most solar wind wave modes to increase in intensity at smaller heliocentric distances. Based on this we can estimate the intensity of the whistler mode emissions at 0.2 AU to be between $10^{-5} \text{ nT} / \sqrt{\text{Hz}}$ and $1 \text{ nT} / \sqrt{\text{Hz}}$ (Gurnett, 1978). These arguments were taken into account in the definition of the characteristics of the SCMs.

Observations made by HELIOS have also revealed the occurrence of ion acoustic-like electrostatic waves in the solar wind at frequencies between the electron and ion plasma frequencies. At 0.2 AU we have $f_{pi} = 4 \text{ kHz}$ and $f_{pe} = 200 \text{ kHz}$. Although the ion-acoustic mode propagates at frequencies below f_{pi} , the observed wave frequencies are primarily determined by their Doppler shift, which is considerably larger than f_{pi} . As pointed out by Kellogg et al. (1999), magnetic field measurements are necessary to unambiguously determine whether the observed waves are electromagnetic or electrostatic. It is worth mentioning that in the presence of shear in the magnetic and velocity fields may lead to the existence of wave modes that have a magnetic component, unlike what would happen in a homogeneous plasma. We estimate the amplitude of these waves to be of the order of $10^{-3} \text{ nT} / \sqrt{\text{Hz}}$, which is large enough to be detected by the SCMs.

Another important scientific objective is particle acceleration in association with Coronal Mass Ejections (CMEs) and flares. Different acceleration mechanisms acceleration can occur, such as the acceleration by collisionless shocks, or associated with the CME propagation such as by a potential electric field along the magnetic field lines. Accelerated electrons generate high frequency electrostatic and electromagnetic waves. Both missions give us the possibility to carry out a systematic study of wave activity in the frequency range (below 10 MHz) that cannot be observed from ground because of the ionospheric cutoff. Such waves have been observed by the Wind satellite, whose observations give excellent examples of radio emissions associated with flares and CMEs propagating in the interplanetary medium (Reiner et al., 2001).

Finally, both missions will also allow to study solar wind turbulence, including the kinetic range, which has received growing interest (Chen, 2016). However, in order to properly resolve the weak levels at kinetic scales a dedicated mission such as Turbulence Heating Observer (THOR) (Vaivads et al., 2016) would be needed with more sensitive instruments. From radial scans that are based on multiple spacecraft (Bruno & Carbone, 2013) we expect the level of turbulence to reach 10^{-5} nT/ $\sqrt{\text{Hz}}$ inside 0.2 AU in the kinetic range.

So far we have concentrated on the smallest expected amplitudes only, which sets the required sensitivity of the instruments. This is the quantity that is plotted in Figure 1. Another issue is the determination of the largest expected amplitude, which determines the gain of the instrument chain and its dynamic range. The latter is much more a concern close to the Sun than in the magnetosphere because the fluctuating wavefield is a mix of quiet intervals and strong transients. This dynamic range is constrained both by the digital resolution (the number of bits) of the analog to digital converter (ADC) and by the gain of the SCM.

Estimating the upper limit of the dynamic range close to the Sun turned out to be a real challenge because of the lack of observations. The closest estimates we could rely on were the sparse observations from the search-coil onboard HELIOS (Neubauer & Musmann, 1977). Multi-spacecraft studies have shown that the level of fluctuations increases close to the Sun because $|\delta B|/|B|$ tends to be invariant with distance R whereas the magnitude of the magnetic field varies as $B \propto R^{-\beta}$ with $\beta = 1.6-2$ (Khabarova & Obridko, 2012). Meanwhile, characteristic scales such as gyroradii decrease with R . Some of the simple scalings may break down closer to the Sun because features such as shocks may not have had time yet to evolve, and so might actually be even steeper.

Since search-coils essentially measure the time derivative of the magnetic field, the combined effect of increasing amplitude and shorter time scales may generate voltages that could potentially saturate the instrumental chain. The maximal levels were intensely debated during the instrument design phase. Eventually, for Parker Solar Probe, we decided to set the upper limit to 3,000 nT at 0.8 kHz in order to be able to capture the largest events.

3. Sensor Definition

Most search-coils that have flown so far on space missions were dedicated to the study of the near-Earth environment, such as Cluster (Cornilleau-Wehrin et al., 2003), the Magnetosphere Multiscale Mission (Le Contel et al., 2014) or the Van Allen probes (Kletzing et al., 2013). Moving into the inner heliosphere brings in new science requirements and also adds new constraints that impact the design of these instruments.

The main science requirements are the measurement of the three components of the fluctuating magnetic field with sufficient sensitivity to capture the different types of waves that are listed in Section 1, namely shocks and transients with wave activity in their close vicinity, plasma waves (e.g. ion-cyclotron, Alfvén, whistler, etc.) and also the background turbulent magnetic field. At the high-frequency end the instrument should be able to measure the magnetic component of radio waves associated with type II and type III radio bursts and mode-converted waves near the Langmuir frequency such as the z-mode (Bale et al., 1998), whose magnetic component has not yet been observed. These types of waves or events and their expected level of amplitude in the inner heliosphere are illustrated in Figure 1.

For Parker Solar Probe, given the maximal amplitude of 3,000 nT at 0.8 kHz the weakest amplitudes are set by the dynamic range of the instrument chain, which is 115 dB. This dynamic range is shorter than the one expected for the fluctuations, which should be approximately 140 dB, see Figure 1. This implies that the weakest waves and in particular turbulence at high frequencies may not be fully resolved.

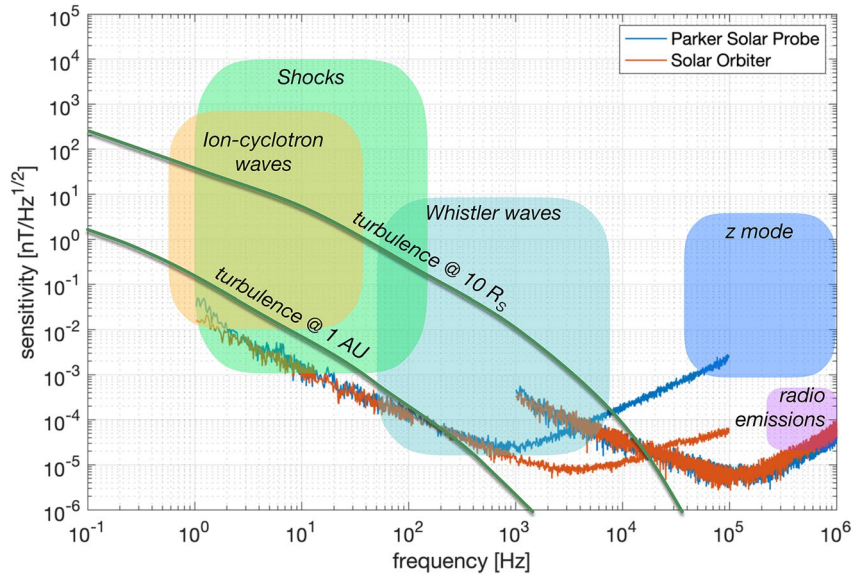


Figure 1. Sensitivity of the SCM sensors for Parker Solar Probe and Solar Orbiter with respect to the expected levels of magnetic fluctuations in the inner heliosphere (for one component of the magnetic field). The levels of turbulence at $10 R_S$ are extrapolated from HELIOS observations made at 0.3 AU.

On Solar Orbiter, the expected dynamic range is shorter and therefore the instrument has a higher gain. Key values are listed in Table 1 with the sensitivity of the SCM for its low-frequency channel (LF) and the medium frequency channel (MF) antennas, and their equivalent in magnetic field amplitude.

Figure 2 compares the fluctuation levels observed by the SCM on Parker Solar Probe during the commissioning phase with that observed earlier by HELIOS. To ease the comparison, we show the average spectral density in three frequency bands versus radial distance from the Sun for the HELIOS search-coil and one value for Parker Solar Probe, when it was at its first perihelion, at 0.166 AU. The dashed $1/R^2$ scaling law confirms the empirical scaling of the intensity with distance. Note that the highest frequency band of the HELIOS search-coil is dominated by noise, hence the apparent saturation at $5 \times 10^{-5} \text{ nT}/\sqrt{\text{Hz}}$. The levels that are measured by Parker Solar Probe mostly correspond to solar wind turbulence with ICW. While these levels may seem weak as compared to the allowed dynamic range of the instrument we note the fluctuations are intermittent; 1% of the amplitudes are at least a factor 20 above the mean level.

Table 1
Sensitivity of the SCM on Parker Solar Probe and Solar Orbiter

	Gain	Parker solar probe		Solar orbiter		Units
		LF Antenna @ 0.8 kHz	MF Antenna @ 100 kHz	LF Antenna @ 2 kHz	MF Antenna @ 100 kHz	
Sensitivity		2.8	470	1,412	1,120	
Noise Level		26	6	8	6	$\text{fT}/\sqrt{\text{Hz}}$
Smallest Meas. Field	Low	± 90	± 0.389	± 0.366	± 0.119	pT
	High	± 6	± 0.097			pT
Largest Meas. Field	Low	$\pm 2,990$	± 12.8	± 3	± 3.9	nT
	High	± 185	± 3.19			nT

Note. Values correspond to the peak of the amplitude response. For the LF antenna, the values are those measured by the DFB (for Parker Solar Probe) or LFR (for Solar Orbiter) spectral analyzer; for the MF antenna they correspond to the TDS waveform analyzer. The smallest measurable magnetic field corresponds to the resolution of the receiver. The largest measurable magnetic field corresponds to maximal input of the receiver. DFB, Digital Fields Board; LF, low-frequency channel; LFR, low-frequency receiver; MF, medium frequency channel; TDS, time domain sampler.

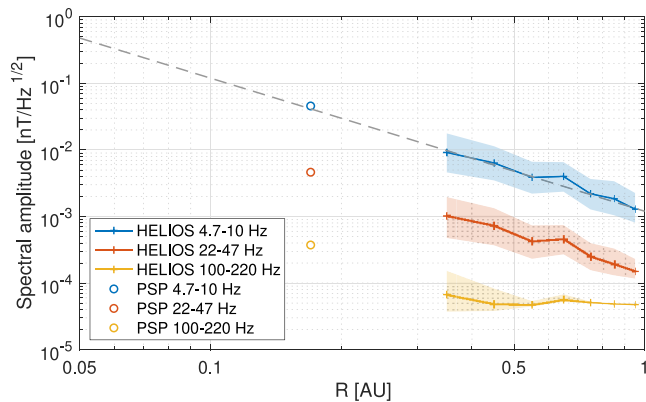


Figure 2. Average spectral amplitude of solar wind turbulence measured by the HELIOS search-coil at various distances from the Sun and by the SCM during the Venus encounter (at 0.5 AU). The dashed area for HELIOS refers to the 25%–75% quantile range. The dashed line represents the expected $1/R^2$ scaling.

Both instruments contain a double-band antenna that covers the MF frequency range in addition to the LF one. Although one single antenna could in principle cover both ranges together, two different antennas that have been individually tuned to their respective frequency bands allow to achieve higher sensitivity.

One of the key challenges with search-coils is their stringent requirement for electromagnetic cleanliness. The requirements for Parker Solar Probe and Solar Orbiter were levied on the instruments and the spacecraft early in the design phase and involved the reduction or shielding of any nearby currents: currents for heating of the fluxgate magnetometers, currents in the solar panels, shielding of the reaction wheels, etc. Such measures, however, usually are not sufficient. For that reason search-coils are located on booms, away from the spacecraft. On Solar Orbiter, the distance to the spacecraft is 2 m whereas on Parker Solar Probe the distance is 3.5 m.

Most search-coils had been accommodated so far on spinning spacecraft (see [Ozaki et al., 2018] for a quasi-exhaustive list), which are more common for missions that focus on *in situ* plasma characteristics. Both Parker Solar Probe and Solar Orbiter, however, are Sun-pointing spacecraft whose search-coils are located in the umbra of the spacecraft. Exposing

the instrument to direct sunlight when the spacecraft is close to the Sun is not allowed because of the scorching heat. The shade, however, adds a new challenge, since without adequate protection the temperature of the instruments would drop below -140 C. To avoid this, the SCMs on Parker Solar Probe and on Solar Orbiter are insulated and heated, see Section 4.4. This unprecedented high temperature difference between the sunlit part of the spacecraft and the SCM sensor located in the shade is not the least of the paradoxes of these two missions.

As of October 2020, both missions have successfully completed their commissioning phase. Parker Solar Probe has already made six perihelion passes (the latest as close to the Sun as 0.095 AU) while Solar Orbiter made its first perihelion pass at 0.52 AU. Both SCM instruments work properly and their first results will be summarized in forthcoming publications. The only issue is a sudden loss since March 2019 of the gain of the LFX channel on Parker Solar Probe. This gain loss is observed whenever the temperature of the instrument drops below 20° C. Unfortunately, low temperature conditions are typically met at perihelion. The most likely cause of is an open circuit in the amplifier output stage.

4. Search-Coil Magnetometer Design

The SCM consists of a compact set of three search-coil antennas that are orthogonally mounted on a non-magnetic support, enabling the measurement of the three components of the fluctuating magnetic field (Hospodarsky, 2016; Pfaff et al., 1998). A preamplifier sends the analog signal through the harness toward the platform where the electronic boxes are located that provide the power supply, the thermal control and perform the digitization and data processing. This preamplifier is located inside of the mechanical structure, the closest possible to the antennas. Thanks to this very compact design, the SCM offers excellent performance for a reasonable mass of typically 550 g, to be compared with 730 g for a similar model on the DEMETER spacecraft (Parrot et al., 2006), and over 1 kg for earlier missions.

The scientific requirements for Solar Orbiter mission are the measurement of the AC magnetic field between a few Hz and 10 kHz with intensities as low as $8 \text{ fT}/\sqrt{\text{Hz}}$ around 2 kHz and a maximum intensity of 5 nT. On Parker Solar Probe the maximum intensity is considerably higher (3,000 nT). Conversely, the smallest intensity is $50 \text{ fT}/\sqrt{\text{Hz}}$ around 2 kHz. Both sensors include one double-band antenna that covers the 10 kHz–500 kHz frequency range for Solar Orbiter and the 10 kHz to 1 MHz range for Parker Solar Probe, with a sensitivity of $50 \text{ fT}/\sqrt{\text{Hz}}$ at 100 kHz. A block diagram of the SCM is shown in Figure 3.

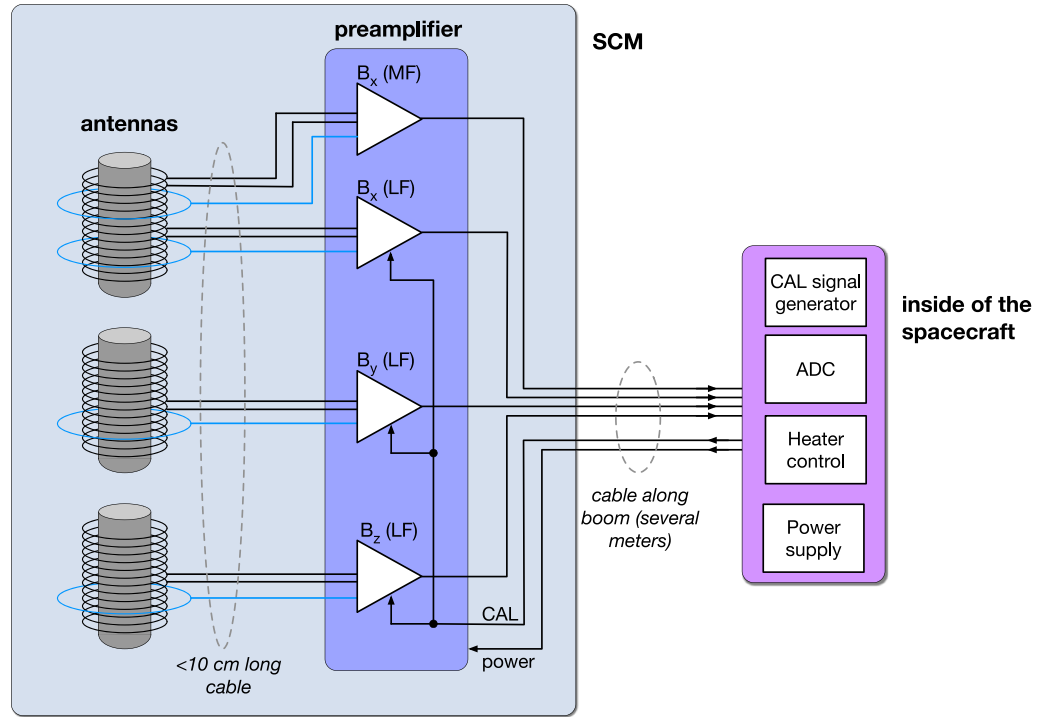


Figure 3. Block diagram of the SCM. The detailed processing of the preamplifier output somewhat differs for Solar Orbiter and for Parker Solar Probe.

4.1. Principle of the Search-Coil Magnetometer

Each antenna of the search-coil measures the component of the magnetic field that is aligned with its axis. The antennas are made of a primary coil with several thousands of turns (depending on the targeted frequency range) wound around a core made of magnetic material. The instrument is based on Faraday's law of induction, which states that a fluctuating magnetic flux Φ passing through a coil with N_1 turns induces a time-varying voltage

$$V = -N_1 \frac{d\Phi}{dt} \quad (1)$$

Taking into account the apparent permeability μ_{app} of the magnetic core, its cross-section S and the component B of the magnetic induction that is parallel to the core, the output voltage on the coil becomes

$$V = -\mu_{app} N_1 S \frac{dB}{dt} \quad (2)$$

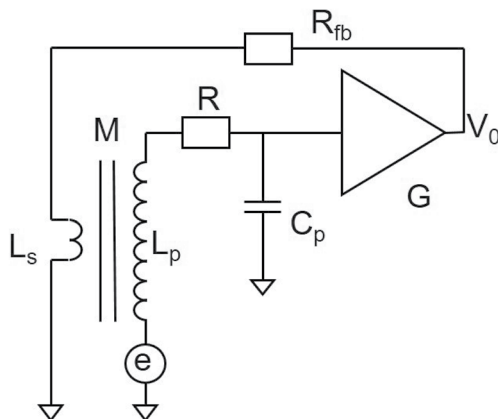


Figure 4. Equivalent circuit of the search-coil antenna and the preamplifier.

The apparent permeability μ_{app} is the ratio between the magnetic field inside the core and the magnetic field outside the core. This parameter depends on the relative permeability of the magnetic material and a demagnetizing factor (Coillot et al., 2009). The output voltage is subsequently preamplified. The equivalent electrical diagram of a one-axis sensor is illustrated in Figure 4. The RLC circuit parameters, L_p , R and C_p are key factors in the design of a search-coil antenna. Table 3 presents the value of these parameters as estimated by calculation and finite element model simulations as well as the measured values for the manufactured antennas. To flatten the frequency response around the resonance frequency (provided that the gain G is high enough) we use a flux feedback coil with

Table 2
Main Parameters of the Search-coil

Main core length, l_c (mm)	100
Main core diameter, d_c (mm)	5
Flux concentrator diameter, d_{fc-ext} (mm)	16
Winding length, l_w (mm)	79
Number of turn per main layer, N_m	831
Number of turn per feedback layer, N_{fb}	9
Number of layers, n	16
Diameter of copper wire, d_{Cu} (μm)	80
Diameter of copper wire with insulator, d_{cw} (μm)	95
Wire resistance, (Ω/km)	3,401
Kapton TM tape thickness, e_k (μm)	45
Length of the mutual reducer, l_{mr} (mm)	60
External diameter of the mutual reducer, d_{mr-ext} (mm)	14
Length of the medium frequency winding, l_{wmf} (mm)	28

Note. These are the parameters that appear in Equations 4–8.

element model with the configuration presented in Figure 5a and using the parameter names and values that are listed in Table 2.

Because of the stringent mass and volume requirements the core length of the antennas was set to 100 mm, which is shorter than most existing search-coils. Longer antennas allow to get better sensitivity, in particular at frequencies below the resonance frequency. For example, the search-coil that had been designed specifically for studying solar wind turbulence at 1 AU in the THOR mission had antennas that were 45 cm long (Vaivads et al., 2016) for a total mass of 2.4 kg. We partly compensated this loss of sensitivity by adding magnetic flux concentrators at the tips of the antennas (Coillot et al., 2009). These diabolo-shaped concentrators allow to increase the apparent permeability of the magnetic core by a factor 1.5 for the design presented here. The material of the core is 3C95 ferrite, which was selected for its better temperature stability compared to the other ferrites we had inventoried. Its magnetic history ($B - H$) relationship was used as input for the solver.

The size of the wire and the number of turns are important parameters for they set the resistance, the inductance and the stray capacitance of the antenna, which in turn need to match the specifications: resonance frequency, noise level, and bandwidth (Séran & Ferreau, 2005). We selected copper wires with a diameter of 80 μm and $N_1 = 13,500$ turns. With these parameters, we typically obtain 16 layers of windings, each of which has a total length of 79 mm. In an effort to reduce the coil self-capacitance, we used the “discontinuous coil” method by Ferrieux and Forest (2006) with a variant on the path leading from one end to the other after each new winding layer: instead of following the recommended straight path, which is more

tricky to do, we applied a small number of turns ($N_{fb} = N_m$) that were equally distributed along the winding length. The total number of turns N_1 of the main coil is thus $N_{fb} + N_m$. One layer of kaptonTM separates the winding layers. The length of the copper wire required for the main coil is

$$\frac{V_0}{B} = R_{fb} \frac{l}{\mu_0 N_2 \lambda} \quad (3)$$

where λ is a correction coefficient that depends on the ratio between the winding length and the core length l ; R_{fb} stands the feedback resistance inside the preamplifier. The flux feedback coil contribution to the electrical model is the inductor L_s .

4.2. Antenna Design

Because Parker Solar Probe and Solar Orbiter missions were assembled almost simultaneously, the search-coils also were and we decided to use the same antennas for both instruments while adapting the preamplifiers to the different specifications. For both instruments the highest sensitivity is achieved near the main resonance frequency $f = (2\pi\sqrt{LC})^{-1}$, which is set by the antenna characteristics and is located near 1 kHz.

The antenna characteristics (magnetic behavior, inductance) were defined by using a two-dimensional magnetostatic axisymmetric finite ele-

ment model with the configuration presented in Figure 5a and using the parameter names and values that are listed in Table 2.

Because of the stringent mass and volume requirements the core length of the antennas was set to 100 mm, which is shorter than most existing search-coils. Longer antennas allow to get better sensitivity, in particular at frequencies below the resonance frequency. For example, the search-coil that had been designed specifically for studying solar wind turbulence at 1 AU in the THOR mission had antennas that were 45 cm long (Vaivads et al., 2016) for a total mass of 2.4 kg. We partly compensated this loss of sensitivity by adding magnetic flux concentrators at the tips of the antennas (Coillot et al., 2009). These diabolo-shaped concentrators allow to increase the apparent permeability of the magnetic core by a factor 1.5 for the design presented here. The material of the core is 3C95 ferrite, which was selected for its better temperature stability compared to the other ferrites we had inventoried. Its magnetic history ($B - H$) relationship was used as input for the solver.

The size of the wire and the number of turns are important parameters for they set the resistance, the inductance and the stray capacitance of the antenna, which in turn need to match the specifications: resonance frequency, noise level, and bandwidth (Séran & Ferreau, 2005). We selected copper wires with a diameter of 80 μm and $N_1 = 13,500$ turns. With these parameters, we typically obtain 16 layers of windings, each of which has a total length of 79 mm. In an effort to reduce the coil self-capacitance, we used the “discontinuous coil” method by Ferrieux and Forest (2006) with a variant on the path leading from one end to the other after each new winding layer: instead of following the recommended straight path, which is more

tricky to do, we applied a small number of turns ($N_{fb} = N_m$) that were equally distributed along the winding length. The total number of turns N_1 of the main coil is thus $N_{fb} + N_m$. One layer of kaptonTM separates the winding layers. The length of the copper wire required for the main coil is

$$l_{wmc} = \pi N_m \sum_{i=1}^n [d_c + (2i - 1)d_{cw} + 2(i - 1)e_k] \quad (4)$$

In which the different parameters refer to those listed in Table 2 and Figure 5.

For the feedback layers, the length is

$$l_{wfb} = \pi N_{fb} \sum_{i=1}^n [d_c + 2id_{cw} + 2(i - 1)e_k] \quad (5)$$

Table 3
Characteristics of the Low-Frequency Search-coil

Parameter	Expected value	Measured value
Number of turns N_1	13,500	13,554
Inductance of the primary coil L_p	11.15 H	10.95 H
Resistance of the primary coil R	1124 Ω	1107 Ω
Capacitance of the primary coil C_p	52 pF	48 pF
External diameter of the winding d_w	9.5 mm	9.9 mm

Note. Expected and measured values (average of the measurements on 10 antennas).

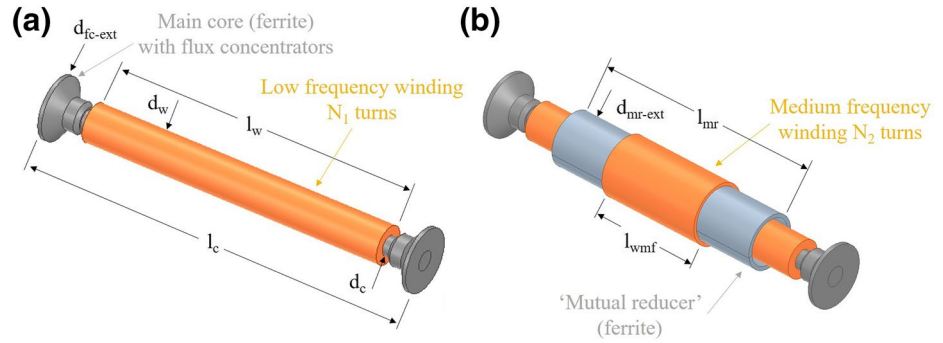


Figure 5. Characteristics of the (a) single band and (b) double band search-coil antennas.

By adding both lengths l_{wmc} and l_{wfb} , we obtain the total length of the coiling wire, which sets the resistance of the coil, using the values that are listed in Table 2.

The external diameter of the windings is estimated from

$$d_w = d_c + 2nd_{cw} + 2ne_k. \quad (6)$$

However, this expression does not take into account the feedback layers whose contribution to the outer diameter is difficult to evaluate since they depend on how the coil is made. The number of turns per layer being large ($N_m > 100$), the major contribution to the coil capacitance (C_p) is the layer-to-layer capacitance (Séran & Fergeau, 2005). After Ferrieux and Forest (2006) we obtain

$$C_p = \frac{6\pi\epsilon_0\epsilon_r l_w}{3e_{in}n^2} \sum_{n=1}^{i=1} r_i, \quad (7)$$

where r_i is the mean radius between 2 consecutive layers, e_{in} is the thickness of the insulator between 2 layers. The insulator is made of the kaptonTM tape (e_k) and the enamel of the coiling wire ($d_{cw} - d_{Cu}$). ϵ_r is the dielectric constant of the insulator, the value of ϵ_r for both materials being similar, 3.4 for kaptonTM and 3.5 for the enamel (given by the manufacturers), the calculation is done with 3.4. Applied to our design, the value of the capacitance then becomes

$$C_p = \frac{\pi\epsilon_0\epsilon_r l_w}{(e_k + d_{cw} - d_{Cu})n^2} (n-1) [d_c + nd_{Cu} + (n-1)(e_k + d_{cw} - d_{Cu})]. \quad (8)$$

To cover the medium frequency band above 10 kHz, the B_x antenna contains an additional coil that is wound around the low-frequency one, as described by Coillot et al. (2009). The low-frequency coil is first covered by two half-cylinders of ferrite with a 1 mm thickness to reduce the mutual inductance between both coils (Figure 5b). The medium frequency coil has $N_2 = 360$ turns and 3 turns for the counter feedback.

Once the winding is done, we wrap each antenna with an electrostatic shield made of a flexible printed circuit that reduces the sensitivity to stray electric fields. Each antenna is then inserted in a carbon fiber tube of 20 mm diameter and 104 mm length, and is potted with a low-density epoxy resin. The final mass is 60 g for single band antennas and 68 g for the double band one. After the manufacturing of the antennas, their characteristics $L_p - R - C_p$ are measured with a HP4294 A impedance analyzer that gives us the equivalent electric circuit. Table 3 shows the good agreement between the expected (modeled) and measured values.

4.3. Preamplifier Design and Manufacturing

The four analog signals that are produced by the three low-frequency antennas and the medium frequency antenna are routed with a very short cable (less than 10 cm) to the preamplifier, which is located inside of the compact mechanical structure of the instrument, the closest possible to the antennas. This is an important point since by reducing that way the cable capacitance (which is not negligible as compared to the coil

Table 4
Physical Characteristics of the SCMs

		Solar Orbiter	Parker Solar Probe
Instrument overall	(without MLI)	ϕ 104 mm,	ϕ 104 mm,
Dimensions		height 158 mm	height 158 mm
Instrument mass	(without MLI)	544 g	563 g
Power consumption	(preamplifier)	195 mW	312 mW
		+12 V/-5V supply	\pm 12V supply
Heating power	(calculated for a boom at -145°C)	1.40 W	1.28 W

MLI, multi-layer insulation.

capacitance) we improve the frequency response. The preamplifier consists of four amplification channels that are adapted to the corresponding frequency range. The baseline used to design the circuits is presented in Séran and Ferreau (2005). Each channel has two stages. The first one, mentioned in Figure 4, consists of a differential pair of JFET transistors achieving a low-noise input associated with a low-power operational amplifier. The gain G of the first stage was set to 50 dB to optimize the counter feedback signal.

As shown in Equation 3, this gain directly depends on the value of the feedback resistance R_{fb} , which is the parameter we adjusted to meet the specifications. For Solar Orbiter, where the maximum intensity of the magnetic field intensity is 5 nT, the value of R_{fb} was set at 15 k Ω to have a high gain of -27 dBV/nT at the output of the first stage. The second stage is a high-pass and low-pass filter with an additional gain of 30 dB, leading to a total gain of 3 dBV/nT (or 1.41 V/nT) at best at the output of the instrument as presented in Figure 9

For Parker Solar Probe, whose maximum intensity is 3,000 nT, the resistance R_{fb} was set to a lower value (1 k Ω), ending up with a gain of -51 dBV/nT at the output of the first stage. The second stage is a high-pass and low-pass filter with unit gain, leading to a total gain of 2.82 mV/nT at the output of the instrument as presented in Figure 9.

We designed the medium frequency channels on a similar basis with the active and passive components adapted to their frequency range from 10 kHz to 500 kHz (respectively, 1 MHz for Parker Solar Probe), see Figure 9. The power consumption is given in Table 4.

By definition, the flux counter feedback should dampen the coil resonance, reduce the risk of having instabilities at nearby frequencies and reduce the sensitivity to parameter variations. However, as a closed loop system, there is a risk of oscillation and instability at higher frequencies outside of the bandwidth, especially when a relatively small value of the counter-feedback resistance R_{fb} is used as is the case for Parker Solar Probe. Figure 6 shows the Nyquist plot of the open loop transfer function of both instruments. Such plots are routinely used to assess the stability of a system with feedback. For Solar orbiter, which represented in green, the value of R_{fb} is high and the system is stable with appropriate gain and phase margins. For Parker Solar Probe (red) the low value of R_{fb} brings the system very close to the point $(-1, 0)$ where instabilities start. During the testing, we detected an oscillation at 210 kHz. To stabilize the system while preserving the antenna design and the desired gain, we shifted the resonance frequency to lower values by introducing a capacitor in parallel with the main coil. The resulting Nyquist curve (in blue) shows that this solution was effective.

Figure 7 shows the preamplifier modules that were designed at LPC2E and manufactured using three-dimensional (3D) technology (hybrid) by the French company 3D Plus. The electronic circuit of each measurement channel is implemented on its own flexible printed circuit board. The circuits are then stacked together in a compact way and molded in resin with pins on the top and bottom faces of the module for the connections respectively to the antennas and to the harness. The module on Parker Solar Probe's is slightly larger because it contains an additional stage with high voltage capacitors. These should protect against deep dielectric discharges that may occur in the spacecraft harnesses because of energetic particles.

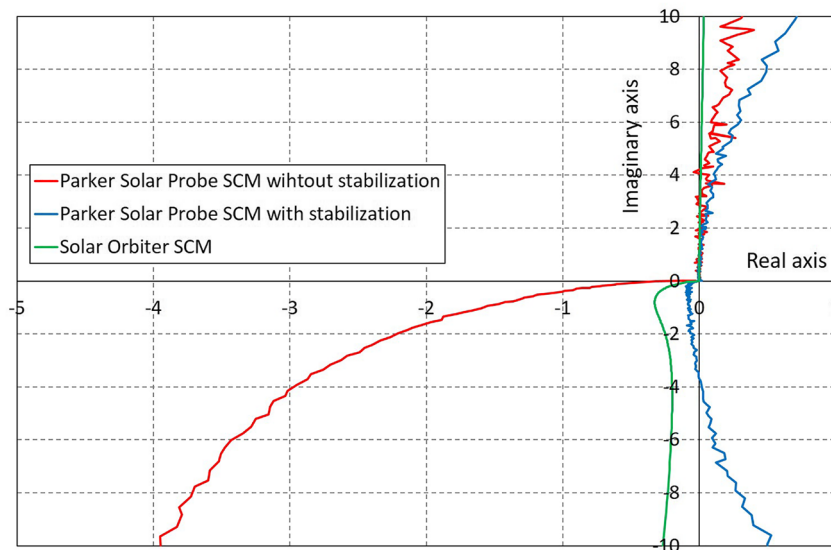


Figure 6. Nyquist plots of SCM open loop transfer functions for the Solar Orbiter (green) and Parker Solar Probe (red) instruments. The loop was open between the first amplification stage and R_{fb} . In this plot the abscissa axis represents the real part of the transfer function and the ordinate axis the imaginary part.

The modules have an octagonal cross-section fitting inside a 18.5 mm diameter circle. The height is 36 mm for Solar Orbiter and 45 mm for Parker Solar Probe. These small dimensions are necessary to make the pre-amplifier fit inside the mechanical structure of the sensor.

4.4. Mechanical Structure and Thermal Interfaces

For both missions, the SCM is located on the spacecraft's deployable boom together with other instruments. For more details on these, see (Bale et al., 2016) for Parker Solar Probe and (Maksimovic et al., 2020) for Solar Orbiter. The boom and the SCM permanently reside in the shade of the spacecraft (except during maneuvers) with temperatures that may drop below -140°C . Such extreme conditions are unusual because the vast majority of search-coils are accommodated on spacecraft that are either spinning or periodically expose them to sunlight.

The low temperatures made the design of the mechanical and thermal interfaces a challenging task. For that reason, considerable attention was paid to the thermal modeling of the thermal interfaces. The model results were compared to the observations thanks to two thermal balance tests performed on the engineering and flight models. Several in-flight configurations have been analyzed but the thermal design was mainly done by considering the coldest operational case. At 1.2 AU with a spacecraft in a Sun-pointing attitude, the SCM unit is exposed to deep space (-270°C) while the boom on which it is mounted is at -145°C . The instrument then operates at nominal power (Table 4) minus a 20% margin. To keep the instrument in its acceptable temperature range, a heater is needed. The challenge is to optimize the thermal design in order to reduce the heating power need. In the worst case configuration, the thermal losses are either radiative (typically 13%) or conducted away through the mounting interface on the boom (53%) and through the harness (33%). To reduce radiative thermal losses, we surrounded the instrument by a thermal blanket made of double thermal multi-layer insulation (MLI) for Solar Orbiter and a single one for Parker Solar Probe. To mitigate conductive losses at the boom interface we used an insulating sole to thermally

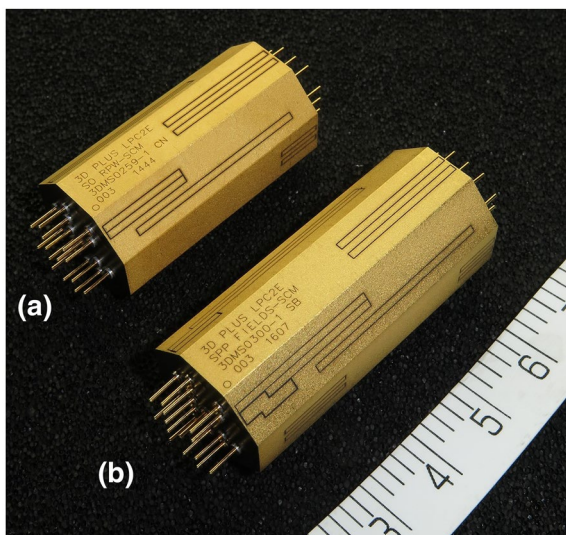


Figure 7. SCM preamplifiers manufactured for Solar Orbiter (a) and Parker Solar Probe (b). The scale is in centimeters.

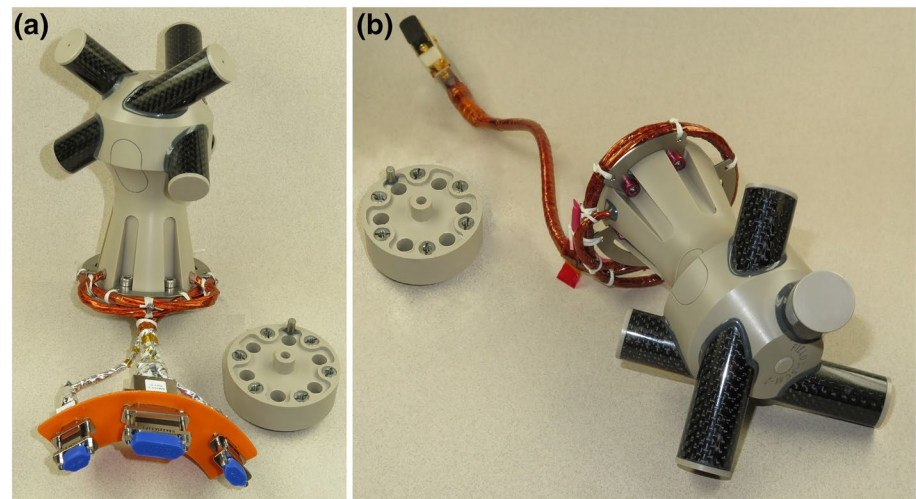


Figure 8. Search-coil magnetometers for (a) Solar Orbiter and for Parker Solar (b) Probe.

decouple the SCM from the boom (see Figure 8) and made one turn with the cables around the instrument (underneath the MLI insulation) before gathering them into pigtails (1 or 3 depending on the satellite) that were then connected to the boom harness. These design modifications enabled to reduce the heating power need of 20%.

The preamplifier is the most sensitive part to temperature excursions. Its location inside of the instrument already provides some thermal protection. In addition, to maintain its temperature above -50°C we wrap it into heaters controlled by the electronic boxes that are located on the spacecraft platform. On both missions these heaters are powered by a sequence of square pulses of 28 V amplitude with a duty cycle that varies as a function of the heating power need. These pulses were not supposed to interfere with the measurements thanks to the careful design of the heaters. Nevertheless, after launch, we noticed a small signature of the heating pulses during periods of low magnetic activity. The signature manifests itself as spikes that coincide with the rising and falling edges of the heater switching on and off. For Solar Orbiter the spike peak intensity is approximately 400 times the resolution of the ADC and its duration is 50 ms. The rate of occurrence depends on the heater activity. The periodicity is typically 80 s at 1 AU and slowly decreases as the temperature increases near the Sun. Clearly, future versions should include additional filtering to remove such interferences by softening the steep edges of the heater pulses.

The compact structure that houses the three orthogonal antennas and the preamplifier is made of Poly-ether ether ketone (unreinforced PEEK) which offered the best trade-off between the mechanical stiffness and the thermal insulation. Indeed, the mechanical structure of the instrument was designed to fulfill at the same time the stringent thermal and mechanical constraints of both missions. The foot is designed to reduce the thermally conductive path between the preamplifier and the boom while ensuring that the structure will be able to withstand the vibrations and the shocks constraints specified by the satellite. Titanium inserts were implemented on the bolted interfaces for that purpose.

The cavity inside of the foot houses the preamplifier in a way that minimizes cable length and so that none of the cables protrudes outside. The assembly of the instrument requires considerable attention as this small cavity ($\phi 25$ mm, height 61 mm) houses, in addition to the preamplifier, a copper tube acting as radiation shielding (wrapped around the electronic module and bearing the heaters), temperature sensors used by the thermal control system and the connections between the preamplifier and the harnesses at the base of the structure.

The SCM was also designed to cope with the radiative environment of the missions. The preamplifier module has tantalum layers of 0.5 mm thickness on the top and bottom octagonal sections. The sides of the preamplifier are shielded by the 1 mm thick copper tube that surrounds it. With these tantalum and copper

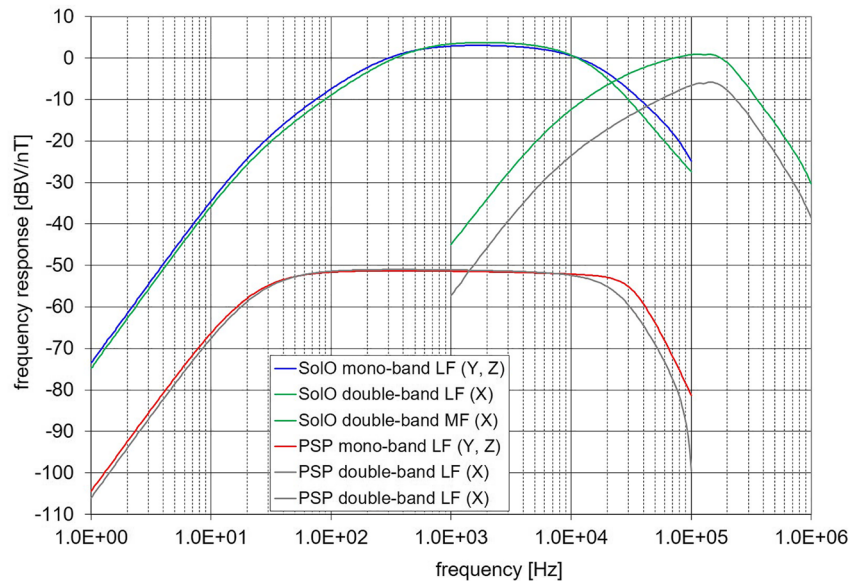


Figure 9. SCM transfer functions (gain) in dBV/nT for the instrument on Solar Orbiter and on Parker Solar Probe.

layers, the preamplifier is fully protected with an equivalent 3 mm of aluminum. Sector analysis based on the environmental specifications of the missions and using FASTRAD™ solver have been performed to evaluate the level of radiation likely to be seen at preamplifier level. With the shielding and the other elements constituting the instrument, the total ionizing dose seen by the preamplifier is reduced from 400 krad with 0.25 mm of equivalent aluminum shielding to 12 krad on Parker Solar Probe and from 200 krad with 0.5 mm of equivalent aluminum shielding to 6 krad on Solar Orbiter. The physical characteristics of the instruments are summarized in Table 4.

5. Instrument Performance

The measured transfer functions for the three LF and MF are presented on Figure 9 for Solar Orbiter and Parker Solar Probe SCM. For both cases, there is a good agreement between the single band antennas on LFy and LFz axis. Differences are observed with the double-band antenna on LFx axis because of the mutual reducer and the medium frequency coil that change the impedance (L_p and C_p) of the low-frequency coil. The value of the counter feedback resistance R_{fb} in the LFx amplification circuit was set to a different value from the two others in order to have similar gains in the frequency band of interest hence the differences mainly observed in the low and high parts of the band.

Figure 10 shows the noise levels or Noise Equivalent Magnetic Induction (NEMI) for both instruments. These measurements were performed at ambient temperature with the instrument operating alone inside a 4-layer mu-metal shielding. For the instrument for Solar Orbiter, the optimum NEMI is $8 \text{ fT}/\sqrt{\text{Hz}}$ obtained at 2 kHz for the low-frequency channels LFy and LFz and is $6 \text{ fT}/\sqrt{\text{Hz}}$ at 100 kHz for the medium frequency channel MFx. As for the frequency response curves, on the double-band antenna, the performances of the low-frequency channel are impacted by the presence of the mutual reducer and the medium frequency coil, the best NEMI being $18 \text{ fT}/\sqrt{\text{Hz}}$. For Parker Solar Probe instrument, the best noise level is $26 \text{ fT}/\sqrt{\text{Hz}}$ at 0.8 kHz for the two single band antennas (LFy and LFz). The impact of the double-band antenna design is also visible since the best measured NEMI is $30 \text{ fT}/\sqrt{\text{Hz}}$ for LFx. For the medium frequency channel, the best measured noise level is $6 \text{ fT}/\sqrt{\text{Hz}}$ at 100 kHz. Compared to the levels observed for Solar Orbiter, the noise level is higher and the minimum is measured at lower frequencies. This is due to the design adaptations to measure higher intensity magnetic fields and to stabilize the system.

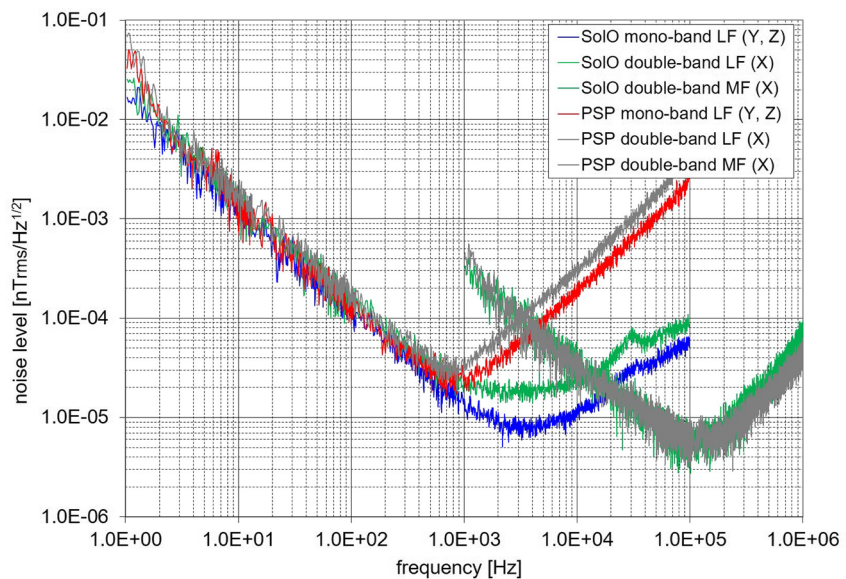


Figure 10. Noise level for the instrument on Solar Orbiter (blue) and on Parker Solar Probe (red).

Measurements by the SCM are in addition influenced by:

- **Cross-talk:** The drawback of having such a light and compact instrument is a higher level of cross-talk between the three antennas (see also Ozaki et al. (2018) for a recent discussion on this issue). For both instruments we measured non-negligible levels of cross-talk in the central part on the frequency band of interest. In the worst case the contribution of a magnetic field perpendicular to an antenna of interest is -26 dB. There is one exception: at the high frequency end of the LFy antenna on Solar Orbiter (around 10 kHz), the contribution from the magnetic field in the X direction reaches -10 dB. This cross-talk primarily comes from the MF part of the antenna.

For Solar Orbiter, however, these effects were fully characterized before launch, allowing us to correct them by performing a matricial calibration. The performances presented on Figure 9 for the measured field in one direction are then preserved. The detailed procedure and resulting in-flight performances will be presented in forthcoming publication.

- **EMC:** Another limitation to the measurement of weak magnetic fields, which is independent of the sensor, is the pollution of the solar wind signal by electromagnetic interference. This important issue is widely known as electromagnetic cleanliness (EMC). Some of these interferences for the SCM were anticipated. In particular, we carried out extensive tests on the ground with the other instruments that are located on the boom (fluxgate magnetometer and for Solar Orbiter only, electron detectors). Tests made with the fluxgate magnetometers allowed us to optimize the separation of the instruments on the boom. The full characterization of the non-natural electromagnetic signals relevant for the instrument performances can only be done in flight and will be presented in separate publications.

6. Data Products

6.1. Data Products for the Parker Solar Probe Mission

On the Parker Solar Probe mission, the analog outputs of the SCM are sent to three different analyzers: the Digital Fields Board (DFB Malaspina et al. [2016]), the time domain sampler (TDS, [Bale et al., 2016]) and potentially also the Radio Frequency Spectrometer (RFS, Pulupa et al. [2017]). DFB produces time series for the three LF antennas only. For all antennas it produces (auto-)spectra, cross-spectra, and band-pass filtered amplitudes with a large variety of operation modes. The sampling rates are given by $150,000 \text{ kHz}/2^n$ where n

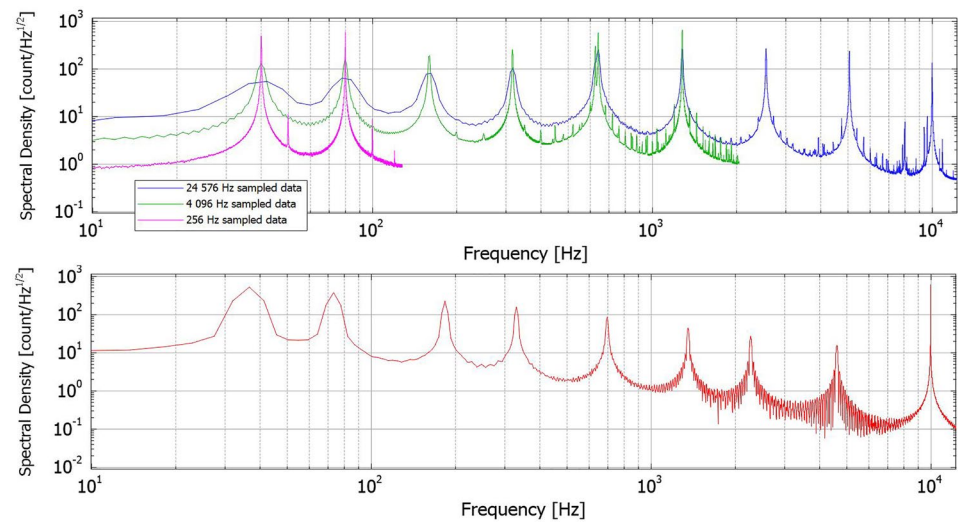


Figure 11. Response of the SCM to the on-board calibration stimulus sampled by the data analyzers LFR on Solar Orbiter (top) and DFB on Parker Solar Probe (bottom).

is an integer. For waveforms the sampling rates vary between a few Hz and 18750 Hz with a typical (survey mode) value of 292.97 Hz. In burst mode, DFB can sample up to 150 kHz.

Spectral and cross-spectral products are available in two frequency ranges: the AC range runs from 366.2 Hz to 72.66 kHz and the DC range from 22.88 Hz to 4,541 Hz. The number of frequency bins can be either 56 or 96. The bandpass filtered data also have two frequency ranges: the AC range goes from 878.9 Hz to 56250 Hz and DC range from 1.717 Hz to 7,031 Hz, with, respectively, 7 and 15 frequency bins.

TDS and RFS both use data from the MF antenna only to produce respectively time series and spectra. The burst waveforms are triggered to detect dust impacts and intermittent waves in the electric field. A product with merged magnetic field from the SCM and MAG fluxgate (Bale et al., 2016) has been developed and is available as a L3 product (Bowen et al., 2020). The merging method is similar to the one used for the fluxgate and search-coil of the Magnetospheric Multiscale Mission (Fischer et al., 2016).

6.2. Data Products of the Solar Orbiter Mission

On Solar Orbiter the analog outputs of the SCM are also sent to three different analyzers (Maksimovic et al., 2020): the low-frequency receiver (LFR), which works in the frequency range from a few Hertz to 12 kHz, the TDS, from 200 Hz to 500 kHz, and the thermal noise and high frequency receiver (THR), which analyzes the signal of the MF antenna from 4 kHz to 1 MHz. In normal mode, LFR produces each 5 min and for each axis, 3 waveform snapshots at $f_0 = 24$ kHz, $f_1 = 4$ kHz, and $f_2 = 256$ Hz. In addition, LFR continuously computes spectra and cross-spectra as well as several wave parameters; see (Maksimovic et al., 2020) for more details. Data from the MF channel are analyzed by TDS and THR. THR computes the power spectrum of up to 980 MHz. In normal mode, TDS produces high cadence waveform snapshots of the MF channel, both regularly (every 5 min) and randomly. As on Parker Solar Probe, TDS can be triggered to detect dust impacts and waves. In case of LFR failure, TDS can also measure waveform of the three low-frequency channels of the SCM.

6.3. On-Board Calibrations

On both missions an on-board calibration mode has been implemented, which is similar to that used on other missions such as the Magnetosphere Multiscale Mission (Le Contel et al., 2014). The DFB on Parker Solar Probe and the LFR on Solar Orbiter generate a signal with a known sequence of different frequencies and send it to the SCM counter-feedback winding through the preamplifier. For Parker Solar Probe, the

signal consists of two sine waves. One of them has a constant frequency of 9.96 kHz while the frequency of the other takes values from $9.96 \text{ kHz}/2^n$, where $n = \{1, 2, \dots, 8\}$ (Malaspina et al., 2016).

On Solar Orbiter, the calibration mode consists in continuously repeating a sequence of 5 successive signals composed of a sum of 2 sine waves at the following frequencies: 10.016 kHz/626 Hz, 5.008 kHz/313 Hz, 2.504 kHz/156.5 Hz, 1.252 kHz/78.25 Hz, and 626 Hz/39.125 Hz. An example of the resulting output signals of the SCM is presented in Figure 11.

In both missions this on-board calibration signal is sent periodically to the SCM (typically once per week during the commissioning phase) and the period can be adjusted by telecommand upon request. The signal recorded on the different receivers allows to characterize the SCM gain response and to a lesser degree the phase response in real conditions. This information is precious to check the health of the instrument and correct, if necessary, any deviation from the calibration that has been performed just before launch. Note that the calibrations signals are sent simultaneously to all antennas and so cannot help correct drifts in the cross-talk.

7. Conclusions

We have presented the twin SCM that are flying on the recently launched Parker Solar Probe and Solar Orbiter missions. These SCMs stand out by their compact size (with 10 cm antennas), low mass, and a design that has been tailored to the harsh thermal environments of the two missions. Each instrument has three antennas, one of which has a second winding to cover higher frequencies. The SCM for Solar Orbiter measures magnetic field fluctuations up to 3 nT with an optimum sensitivity of $8 \text{ fT}/\sqrt{\text{Hz}}$ at 2 kHz whereas for Parker Solar Probe it measures fluctuations up to 3,000 nT with an optimum sensitivity of $26 \text{ fT}/\sqrt{\text{Hz}}$ at 0.8 kHz. These sensitivities have been tuned to meet the expected amplitudes of the different types of waves (whistler, ion-cyclotron, etc.) and transients in the inner heliosphere.

The double-band antenna extends the frequency range up to 1 MHz with a Noise Equivalent Magnetic Induction of $6 \text{ fT}/\sqrt{\text{Hz}}$ at 100 kHz and allow to measure fluctuations associated with Langmuir-like waves and Solar radio bursts. The commissioning and science results from the two instruments will be addressed in forthcoming publications.

After decades of gradual improvements and tweaks, search-coils have probably reached their limit in terms of sensitivity versus mass and size. The SCMs for Parker Solar Probe and Solar Orbiter highlight the importance of carefully optimizing each instrument to the science requirements while taking into account the thermal environment. SCMs on outer planetary missions such as ESA's Jupiter Icy Moons Explorer (JUICE) will face different constraints such as high radiation doses. Two major challenges awaiting future instruments are a more modular design to reduce cost and assembly time, and the ability to operate in a broader temperature range. The latter is particularly important since most of the power consumption (at least for missions for which the instrument receives no direct sunlight) goes into heating the instrument and not into operating it.

Another and continuous challenge is the stringent requirement for electromagnetic cleanliness. A sensitive search-coil is worthless if its measurements are polluted by interferences from the spacecraft and from nearby instruments. While careful anticipation during the design and assembly phase of the spacecraft is crucial, keeping the instrument away from the spacecraft, on a long boom, is also vital. New breakthroughs may be expected here with new boom designs.

Data Availability Statement

The development and exploitation of the two SCMs is funded by CNES. Parker Solar Probe was designed, built, and is now operated by the Johns Hopkins Applied Physics Laboratory as part of NASA's Living with a Star (LWS) program (contract NNN06AA01 C). Support from the LWS management and technical team has played a critical role in the success of the Parker Solar Probe mission. All the data used in this work are available on the FIELDS data archive (<http://fields.ssl.berkeley.edu/data/>). Solar Orbiter is a space mission of international collaboration between ESA and NASA. Solar Orbiter data are available at <http://soar.esac.esa.int/soar/>.

Acknowledgments

The SCM team is grateful to the entire FIELDS and RPW teams and to scientists and engineers at LESIA and SSL who participated in reviews and discussions. We specifically thank Jean-Yves Prado, Kader Amsif, Isabelle Fratter and François Gonzalez from the French Space Agency (CNES) for their continuing support. We would like to extend our thanks to CNES people for their technical support on thermal and mechanical design and on PA/QA issues as well as HENSOLDT Space Consulting. The authors would also like to thank the teams of RPW Operations Center (ROC) on Solar Orbiter and FIELDS Science Operations Center (SOC) on Parker Solar Probe. We are indebted to the MAG teams from NASA/GSFC, Imperial College, and Technical University of Braunschweig for performing electromagnetic cleanliness tests with the SCM and to S.E. Harris from SSL for his contributions during the early phase of PSP. We also acknowledge O. Le Contel (LPP) who accepted to review the SCM design and development status for the PSP project key points.

References

Bale, S. D., Goetz, K., Harvey, P. R., Turin, P., Bonnell, J. W., Dudok de Wit, T., et al. (2016). The FIELDS Instrument Suite for Solar Probe Plus. *Space Science Reviews*, 204(49), 1–34. <https://doi.org/10.1007/s11214-016-0244-5>

Bale, S. D., Kellogg, P. J., Goetz, K., & Monson, S. J. (1998). Transverse z-mode waves in the terrestrial electron foreshock. *Geophysical Research Letters*, 25, 9–12. <https://doi.org/10.1029/97GL03493>

Bowen, T. A., Bale, S. D., Bonnell, J. W., Dudok de Wit, T., Goetz, K., Goodrich, K., et al. (2020). A Merged Search-Coil and Fluxgate Magnetometer Data Product for Parker Solar Probe FIELDS. *Journal of Geophysical Research*, 125(5), e2020JA027813. <https://doi.org/10.1029/2020JA027813>

Bruno, R., & Carbone, V. (2013). The Solar Wind as a turbulence laboratory. *Living Reviews in Solar Physics*, 2, 4. <https://doi.org/10.12942/lrsp-2013-2>

Chen, C. H. K. (2016). Recent progress in astrophysical plasma turbulence from solar wind observations. *Journal of Plasma Physics*, 82(6), 535820602. <https://doi.org/10.1017/S0022377816001124>

Coillot, C., Moutoussamy, J., Lebourgeois, R., Ruocco, S., & Chanteur, G. (2009). Principle and performance of a dual-band search coil magnetometer: A new instrument to investigate fluctuating magnetic fields in space. *IEEE Sensors Journal, Institute of Electrical and Electronics Engineers*, 10(2), 255–260. <https://doi.org/10.1109/JSEN.2009.2030977>

Cornilleau-Wehrlin, N., Chanteur, G., Perraut, S., Rezeau, L., Robert, P., Roux, A., et al. (2003). First results obtained by the Cluster STAFF experiment. *Annales Geophysicae*, 21, 437–456.

Ferrière, J., & Forest, F. (2006). *Alimentations à découpage—Convertisseurs à résonance* (3rd ed.). Paris: Editions Dunod.

Fischer, D., Magnes, W., Hagen, C., Dors, I., Chutter, M. W., Needell, J., et al. (2016). Optimized merging of search coil and fluxgate data for mms. *Geoscientific Instrumentation, Methods and Data Systems*, 5(2), 521–530. <https://doi.org/10.5194/gi-5-521-2016>

Fox, N. J., Velli, M. C., Bale, S. D., Decker, R., Driesman, A., Howard, R. A., et al. (2015). The solar probe plus mission: Humanity’s first visit to our star. *Space Science Reviews*, 204, 1–42. <https://doi.org/10.1007/s11214-015-0211-6>

Gurnett, D. A. (1978). Plasma waves near the sun: Advances possible with a solar probe. In M. Neugebauer & R. W. Davies (Eds.), *A close-up of the Sun*. JPL.

Hospodarsky, G. B. (2016). Spaced-based search coil magnetometers. *Journal of Geophysical Research*, 121(A10), 12. <https://doi.org/10.1002/2016JA022565>

Jagarlamudi, V. K., Alexandrova, O., Berčić, L., Dudok de Wit, T., Krasnoselskikh, V., Maksimovic, M., & Štverák, Š. (2020). Whistler waves and electron properties in the inner Heliosphere: HELIOS Observations. *The Astrophysical Journal*, 897(2), 118. <https://doi.org/10.3847/1538-4357/ab94a1>

Kellogg, P. J., Goetz, K., Monson, S. J., & Bale, S. D. (1999). Langmuir waves in a fluctuating solar wind. *Journal of Geophysical Research*, 104, 17069–17078. <https://doi.org/10.1029/1999JA900163>

Khabarova, O., & Obridko, V. (2012). Puzzles of the interplanetary magnetic field in the inner heliosphere. *The Astrophysical Journal*, 761(2), 82. <https://doi.org/10.1088/0004-637X/761/2/82>

Kletzing, C. A., Kurth, W. S., Acuna, M., MacDowall, R. J., Torbert, R. B., Averkamp, T., et al. (2013). The Electric and Magnetic Field Instrument Suite and Integrated Science (EMFISIS) on RBSP. *Space Science Reviews*, 179, 127–181. <https://doi.org/10.1007/s11214-013-9993-6>

Le Contel, O., Leroy, P., Roux, A., Coillot, C., Alison, D., Bouabdellah, A., et al. (2014). The search-coil magnetometer for mms. *Space Science Reviews*, 199, 1–26. <https://doi.org/10.1007/s11214-014-0096-9>

Lefevre, F., Blanc, E., Pinçon, J.-L., Roussel-Dupré, R., Lawrence, D., Sauvaud, J.-A., et al. (2008). TARANIS—A Satellite Project Dedicated to the Physics of TLEs and TGFs. *Space Science Reviews*, 137(1–4), 301–315. <https://doi.org/10.1007/s11214-008-9414-4>

Maksimovic, M., Bale, S., Chust, T., Khotyaintsev, Y., Krasnoselskikh, V., Kretzschmar, M., et al. (2020). The Solar Orbiter Radio and Plasma Waves (RPW) instrument. *Astronomy and Astrophysics*, 642, A12. <https://doi.org/10.1051/0004-6361/201936214>

Malaspina, D. M., Ergun, R. E., Bolton, M., Kien, M., Summers, D., Stevens, K., et al. (2016). The digital fields board for the fields instrument suite on the solar probe plus mission: Analog and digital signal processing. *Journal of Geophysical Research: Space Physics*, 121(6), 5088–5096. <https://doi.org/10.1002/2016JA022344>

Müller, D., Marsden, R. G., Cyr, O. C. St, & Gilbert, H. R. (2013). Solar Orbiter. Exploring the Sun-Heliosphere Connection. *Solar Physics*, 285, 25–70. <https://doi.org/10.1007/s11207-012-0085-7>

Neubauer, F. M., & Musmann, G. (1977). Fast magnetic fluctuations in the solar wind - HELIOS I. *Journal of Geophysical Research*, 82, 3201–3212. <https://doi.org/10.1029/JA082i022p03201>

Ozaki, M., Yagitani, S., Kasahara, Y., Kojima, H., Kasaba, Y., Kumamoto, A., et al. (2018). Magnetic Search Coil (MSC) of Plasma Wave Experiment (PWE) aboard the Arase (ERG) satellite. *Earth Planets and Space*, 70(1), 76. <https://doi.org/10.1186/s40623-018-0837-1>

Parrot, M., Benoist, D., Berthelier, J. J., Blck, J., Chapuis, Y., Colin, F., et al. (2006). The magnetic field experiment IMSC and its data processing onboard DEMETER: Scientific objectives. *description and First Results*, 54(5), 441–455. <https://doi.org/10.1016/j.pss.2005.10.015>

Pfaff, R. F., Borovsky, J. E., & Young, D. T. (1998). *Measurement techniques in space plasmas—Fields*. *Geophysical Monograph Series*. (Vol. 103). Washington, DC: American Geophysical Union.

Pierrard, V., Maksimovic, M., & Lemaire, J. (2001). Core, Halo and Strahl Electrons in the Solar Wind. *Astrophysics and Space Science*, 277, 195–200. <https://doi.org/10.1023/A:1012218600882>

Porsche, H. (1981). HELIOS mission: Mission objectives, mission verification, selected results. In: W. R., Burke(Ed.), *Solar system and its exploration*. (Vol. 164). ESA Special Publication.

Pulupa, M., Bale, S. D., Bonnell, J. W., Bowen, T. A., Carruth, N., Goetz, K., et al. (2017). The solar probe plus radio frequency spectrometer: Measurement requirements, analog design, and digital signal processing. *Journal of Geophysical Research: Space Physics*, 122(3), 2836–2854. <https://doi.org/10.1002/2016JA023345>

Reiner, M. J., M. L. Kaiser, and J.-L. Bougeret (2001). Radio signatures of the origin and propagation of coronal mass ejections through the solar corona and interplanetary medium. *Journal of Geophysical Research*, 106, 29989–30000. <https://doi.org/10.1029/2000JA002228>

Séran, H. C., & Ferreau, P. (2005). An optimized low-frequency three-axis search coil magnetometer for space research. *Review of Scientific Instruments*, 76(4), 044502. <https://doi.org/10.1063/1.1884026>

Tu, C.-Y., & Marsch, E. (2001). Wave dissipation by ion cyclotron resonance in the solar corona. *Astronomy and Astrophysics*, 368, 1071–1076. <https://doi.org/10.1051/0004-6361:20010019>

Vaivads, A., Retinò, A., Soucek, J., Khotyaintsev, Y. V., Valentini, F., Escoubet, C. P., et al. (2016). Turbulence Heating ObserveR – Satellite mission proposal. *Journal of Plasma Physics*, 82(5), 905820501. <https://doi.org/10.1017/S0022377816000775>

Viall, N. M., & Borovsky, J. E. (2020). Nine outstanding questions of solar wind physics. *Journal of Geophysical Research: Space Physics*, 125(7), e2018JA026005. <https://doi.org/10.1029/2018JA026005>